

# Doubly Reinforcing Cementitious Beams with Instrumented Hollow Carbon Fiber Tendons

K.R. Biszick · J.A. Gilbert · H.A. Toutanji ·  
M.T. Britz

Received: 30 November 2011 / Accepted: 1 August 2012 / Published online: 22 August 2012  
© Society for Experimental Mechanics 2012

**Abstract** Surface mounted strain gages are used to characterize the behavior of polymer-enhanced cementitious beams designed to withstand reverse loadings. These unique composite structures are doubly reinforced with hollow carbon fiber (graphite) tendons equipped with strain gages and the study includes section design, materials considerations, structural testing, and finite element analysis. The primary purpose of strain gage integration is to insure that the stress in the materials remains within the elastic range so that damage does not occur. A finite element model is developed to characterize the structural response in the elastic range and a hybrid approach is suggested in which displacement, strain, and stress can be obtained with a single strain gage. The ability to characterize structural performance beyond the elastic range is also demonstrated by analyzing data obtained from displacement-controlled tests.

**Keywords** Structural health monitoring · Doubly reinforced beams · Cementitious materials · Strain gages · Hybrid analysis

## Introduction

Reinforced concrete beams are an important example of structural members made of two different materials. In many cases, these structures are subjected to a static bending moment which places the region below the neutral axis in tension. In these cases, the beams are typically strengthened by placing steel rods a short distance from the lower face. Since concrete is weak in tension, it will crack below the neutral surface and the steel rods will carry the entire tensile load, while the upper portion of the concrete beam will carry the compressive load. However, this design does not work well when the bending moment is reversed, since cracks develop in the unreinforced tensile zone.

The ability of a reinforced concrete structure to resist reverse loadings which may be caused by seismic or wind loads is important and new designs which make this possible may lead to applications ranging from morphing structures to energy harvesting devices. This paper discusses a next generation composite technology which relies on placing a highly flexible polymer-enhanced cementitious matrix over a relatively stiff reinforcement so that reverse bending moments can be sustained. In stark contrast to the construction scenario mentioned above, reinforced concrete beams are fabricated by placing hollow, graphite tendons in the composite section so that it is doubly reinforced. The relatively high stiffness ratio associated with the materials facilitates stress transfer from the concrete to the reinforcement which helps prevent cracks from occurring in the concrete.

At the same time, four strain gages are used to characterize structural behavior. Two of the gages are mounted on the upper and lower concrete surfaces while the other two are mounted on the inner surfaces of the hollow tendons used to reinforce the beam. In practical applications, the strain gages would be monitored to insure that the stress in the materials remained within the elastic range so that damage did not

---

K.R. Biszick  
Optechnology, Inc.,  
5000 Allendale Drive,  
Huntsville, AL 35811, USA

J.A. Gilbert (✉) · M.T. Britz  
Department of Mechanical and Aerospace Engineering,  
University of Alabama in Huntsville,  
Huntsville, AL 35899, USA  
e-mail: jag@eng.uah.edu

H.A. Toutanji  
Department of Civil and Environmental Engineering,  
University of Alabama in Huntsville,  
Huntsville, AL 35899, USA

occur. A finite element model is developed to characterize the structural response in the elastic range and a hybrid approach is suggested in which displacement, strain, and stress can be obtained globally by monitoring a single strain gage.

The ability to characterize structural performance beyond the elastic range is also demonstrated by analyzing data obtained from displacement-controlled tests. Splices in the tendons and slippage between them and the cementitious matrix help to prevent sudden collapse and allow the composite structure to withstand relatively high service loads despite appreciable deformation.

As explained below, the study represents an extension of prior research in the area of polymer-enhanced reinforced cementitious composites and is unique in that 1) a structural information system is developed to characterize the response of a doubly reinforced concrete structure designed to sustain reverse bending, 2) strain gages are placed within hollow carbon fiber tendons, 3) expansion joints are incorporated into the primary reinforcement, and 4) a hybrid approach is suggested.

## Composite Technology

Today's common advanced composite materials are made of continuous fibers (graphite, glass, or Kevlar®) suspended in a polymeric matrix, typically an epoxy of some type [1]. Typical examples include Toray T-300 3 k/934 plain weave fabric and AS4-12 k/3502 unidirectional tape [2].

The technology underlying these materials has been developed over the past sixty years and the materials have been widely used for applications in civil and aerospace engineering primarily due to their high strength-to-weight and/or stiffness-to-weight ratio. In the construction industry, for example, applications range from non-structural gratings and claddings to full structural systems for industrial supports, buildings, long span roof structures, tanks, bridge components, and complete bridge systems [3].

While advances in such composite materials have been steady, there have been relatively few revolutionary changes of late. But the investigation and development of a new breed of polymer-enhanced cementitious composite structures with matrices based on a unique hybrid blend of inorganic and organic components has the potential to revolutionize structural design.

## Polymer-Enhanced Reinforced Cementitious Composites

Although the designs associated with this relatively new technology are based on the strength and position of the

materials in the composite section, the overall design strategy relies mainly on the large difference in stiffness between the constituents in the composite section to drive the internal stress from the matrix to the reinforcement [4]. In more conventional concrete structures reinforced with steel, for example, the ratios of the stiffness of the reinforcement to that of the matrix are about 10. In advanced aerospace composites this ratio is on the order of 100. The greater stiffness ratios associated with polymer-enhanced cementitious structures offer design engineers even more flexibility.

The evolution of this technology began with the production of thin, lightweight, and structurally efficient panels capable of resisting stresses produced by reverse bending [5]. The study showed that a very efficient composite structure having a stiffness ratio equal to 273 could be fabricated by placing a flexible polymer-enhanced cementitious matrix having a low elastic modulus (758 MPa) over two layers of a rigid steel wire mesh having a relatively high elastic modulus (207 GPa).

Materials were placed symmetrically to form a doubly reinforced section that reacted similarly when bending couples were reversed. Since the tensile strength of concrete is much less than its compressive strength (typically on the order of 10 %), it was the tensile strength of the concrete, as well as the modulus of elasticity and bond strength between the matrix and the reinforcement, that impacted the design most.

A modified transform section theory was developed to determine the deflections and stresses in these highly compliant, steel-reinforced, cementitious structures and the method was subsequently applied to study beams reinforced with layers of graphite mesh [6]. At the same time, efforts were made to increase the tensile to compressive strength ratio of the concrete.

In the beams reinforced with layers of graphite mesh, for example, the cementitious material had a tensile strength of 1.77 MPa and a compressive strength of 4.80 MPa, making the ratio 37 % [6]. Symmetrical and unsymmetrical, multi-layered composites were analyzed by incorporating material properties established from standard tests and finite element modeling was used to verify results for composite beams having stiffness ratios equal to 286.

This study led to another investigation which quantified the dynamic characteristics of laminated plates reinforced with graphite mesh [7]. In this study, an analytical dynamic finite element model was developed to evaluate the natural frequencies and mode shapes for structures subjected to different boundary conditions. The model was subsequently applied to study the dynamic performance of a larger laminated structure [8]. Numerical results compared favorably with experimental impact hammer test data. As a result, it was concluded that the classical laminated plate theory developed for composite materials could be applied to

quantify the dynamic behavior of highly compliant composite structures made from cementitious materials.

Research performed on a concrete having a higher modulus than the one described above showed that material deficiencies caused by impact could be overcome by introducing a stiff weave-like reinforcement [9]. Tests were performed on similar sections built with the more compliant matrix to characterize their impact properties [10].

Other impact tests [11] were conducted on cementitious matrices that capitalized on the atomic and molecular interaction which occurred between constituents [12]. The addition of polyvinyl butyral (referred to as PVB and also known as Butvar), for example, created hydrogen bonds which formed between molecules or within different parts of a single molecule. This helped to strengthen the matrix and improved the bonds which formed between it and free fibers used for reinforcement [13, 14]. As illustrated in the present study, a similar strategy can be used to strengthen a doubly reinforced structure outfitted with carbon fiber rebar.

### Employing Instrumented Hollow Carbon Fiber Tendons

Although research in the area of polymer-enhanced cementitious composites has progressed, most of the investigators mentioned above relied on layers of continuous graphite fiber mesh to reinforce relatively thin walled sections. However, there is merit associated with embedding rebar into thicker concrete beams, especially if the rebar can be outfitted with strain gages capable of monitoring the overall performance of the structure.

Many studies have been performed on traditional reinforced concrete structures by placing strain gages directly on the surface of rebar. In these cases, the lead wires are typically wrapped around the rebar and fed to the measuring instrument. As such, the wires are embedded in the surrounding matrix making them susceptible to lead wire effects.

As illustrated in Fig. 1, strain gages have been installed within hollow steel rebar and sister bars [15]. The rebar is embedded directly into the matrix for structural purposes while the sister bar is installed by tying it alongside an existing length of rebar in the rebar cage. Several bars can be joined by screwing them together.



**Fig. 1** RocTest Telemac's instrumented rebar (top) and sister bar (bottom) [15]

Other vibrating wire sister bar strain meters have been used in concrete structures such as piles, diaphragm/slurry walls, bridge abutments, tunnel lining, dams, and foundations [16]. Gages have even been embedded within a membrane to monitor the effects associated with waterproofing roof systems of large buildings [17].

An alternative to producing instrumented steel rebar is to manufacture instrumented hollow carbon fiber reinforced polymer tendons that have strain gages mounted within them [18–20]. In addition to capitalizing on the hydrogen bonding mentioned earlier, the advantages of using graphite as opposed to steel are that graphite is less susceptible to corrosion [21] and it is ten times stronger and five times lighter than steel [22, 23].

This paper discusses the design considerations used to produce a system capable of monitoring the structural behavior of polymer-enhanced cementitious beams designed to withstand reverse loadings. The load reversals may occur due to service loads or natural events such as earthquakes or hurricanes. The doubly reinforced composite section is reinforced with hollow carbon fiber tendons equipped with strain gages and the study includes section design, materials considerations, structural testing, and finite element analysis.

### Section Design

In the present study, tests were conducted on reinforced cementitious beams in accordance with ASTM C78/C78M-10 [24], the standard for determining flexural strength of concrete in third-point loading. Figure 2 shows a schematic diagram of the beam along with its supports.

The height and width of the beam were 0.0889 m and the total length of the reinforced concrete section was 0.5334 m. This allowed a four point bend test to be conducted over a 0.4572 m long span comprised of three equally distant

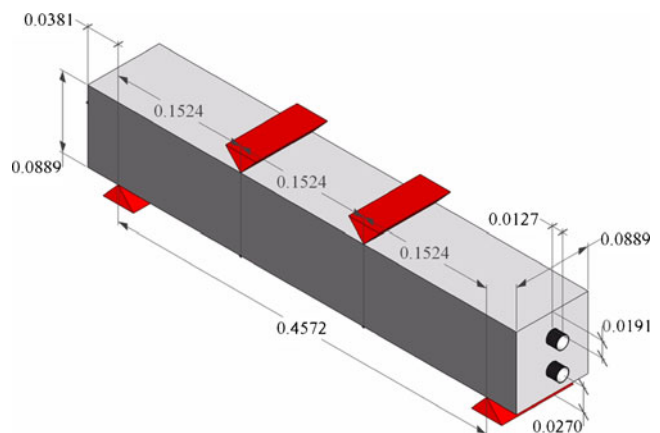


**Fig. 2** Schematic diagram of the four point bend test (dimensions are in meters)

0.1524 m long sections. The central span constituted the constant moment section of the beam where measurements were made. A doubly reinforced section was constructed by placing two instrumented tendons symmetrically in the section; one above, the other below, the neutral axis.

As illustrated in Fig. 3, each tendon consisted of two equal length sections of carbon fiber tubing which were spliced together at the center of the beam to facilitate strain gage placement. Each of the 17.92 mm diameter outer tubes had a wall thickness of 1.02 mm and an inner diameter of 15.88 mm. The 50.8 mm long, 15.65 mm diameter splice was constructed by machining down the outer surface of a different carbon fiber tube which had an inner diameter of 13.97 mm.

A pre-wired, uniaxial strain gage (Omega Type KFG-3-350-C1-11L3M3R) was placed in the longitudinal direction on the inner surface of one of the outer tubes before the splice was inserted and glued in place. The gage was located adjacent to the splice, at a distance of 26.0 mm from the center span of the beam and the lead wires from the gage were fed through the hollow tendon to a data acquisition system.

The instrumented tendons were suspended within a wooden mold so that a polymer-enhanced cementitious mix could be placed over them. Prior to placing concrete around them, the top and bottom tendons were rotated so that the embedded gages were located at the furthest distances from the centroid of the composite section. Referring to Figs. 2 and 3, the upper tendon was rotated until the strain gage was positioned at the top closest to the top concrete surface whereas the lower tendon was rotated until the strain gage was positioned at the bottom closest to the bottom concrete surface. After the reinforced beams had cured, uniaxial strain gages were placed longitudinally at mid span on the top and bottom concrete surfaces of the beam.

## Materials Considerations

Various options were considered for producing hollow tendons ranging from wrapping graphite around a mandrel and vacuum bagging to depositing tape within a female mold and applying internal pressure. After considering the advantages

and disadvantages of these approaches relative to labor and cost, as well as the embedment of strain gages, it was decided to retrofit commercially available graphite tubes.

The graphite tendons and splices were constructed from stock tubing. Each tube was fabricated using multiple layers of AS4/3501-6 unidirectional tape. Although the lamina material properties listed in Table 1 were identified [22, 25, 26], no information was available regarding the ply thickness and stack up (number of plies and fiber orientation). Since the latter was needed to model the composite beam, a diagnostic study was performed to obtain it.

Figure 4 shows a photograph taken during the first step in this process where the outer tube was torched to determine the composition in its wall.

As shown in Fig. 5, there were seven 0.127 mm thick layers of carbon fiber and an outer layer of glass. The fibers in the six outermost carbon fiber layers were oriented at  $0^\circ$  with respect to the longitudinal axis of the tube while those in the innermost layer were oriented circumferentially (at  $90^\circ$ ). The tube used for the splice was similar in construction but the outermost glass layer as well as a portion of the underlying carbon fiber layer was removed so that the splice could fit within the outer tube.

The structural performance of the outer tube was studied prior to constructing the tendons [18]. The photograph in Fig. 6, for example, shows the experimental set up used to measure the center deflection of a 0.305 m long section of the tube placed in pure bending.

In that experiment, the tube was simply supported and bent by applying loads at the ends of adjoining 89 mm long sections. Loads were varied over a limited range to check that the material properties listed in Table 1 and the composite lay-up determined from the diagnostic study were suitable for finite element modeling.

Figure 7 shows a load vs. deflection plot. The solid line labeled experimental corresponds to the measurements taken while the dotted line labeled analytical was generated based on the tube geometry and an equivalent longitudinal modulus equal to 105.2 GPa. The latter was determined based on classical laminated plate theory by using a commercially available program called “The Laminator” [27].

The glass layer contained helically wound grooves designed to prevent slippage between the tube and the

**Fig. 3** Central section of an instrumented tendon (dimensions in millimeters; see Fig. 5 for Section a-a')

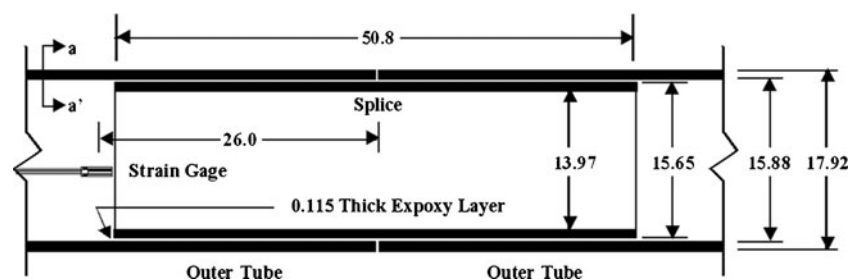


**Table 1** Lamina properties for AS4/3501–6

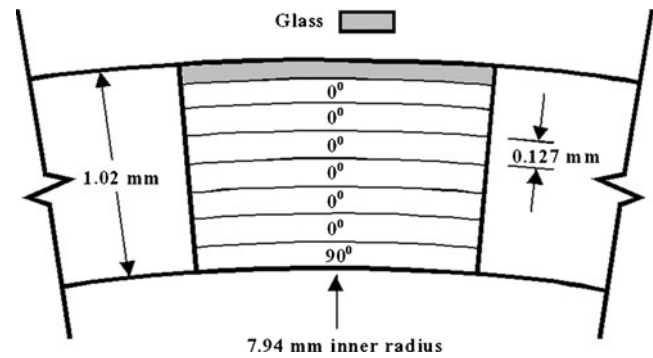
Prepreg resin content (% by wt) [22]	28–38
Fiber volume (%) [22]	60
Transverse modulus (GPa) [22]	10.2
Flexural longitudinal modulus (GPa) [25]	127.6
Longitudinal shear modulus (GPa) [26]	4.3
Transverse shear modulus (GPa) [26]	3.2
Longitudinal poisson's ratio [26]	0.253

surrounding cementitious matrix. During the analysis, this layer was neglected, since it provided negligible strength and stiffness relative to the other carbon fiber lamina. Input to the program consisted of the ply material properties and material strengths listed in Table 1 as well as the ply fiber orientation and stacking sequence illustrated in Fig. 5.

The output parameters from “The Laminator” are listed in Table 2. The close agreement between the experimental and theoretical results indicated that the input parameters were acceptable.

A comprehensive trial and error mix design process was followed to arrive at the final mix proportions for the polymer-enhanced cementitious matrix used to fabricate the beams (see Table 3). The relatively lightweight mix was designed to capitalize on the atomic and molecular interactions which occur between the constituents, and between the matrix and reinforcement, to improve strength and bonding in the composite section [12–14].

Referring to Table 3, the cement was ASTM Type I normal white Portland cement conforming to ASTM C150/C150M-11 [28]. The high-reactivity metakaolin (HRM), which conformed to ASTM C618-08A [29], is a highly processed reactive pozzolan made from purified kaolin clay. With a particle size smaller than that of cement, metakaolin is a white, amorphous, aluminosilicate that reacts aggressively with calcium hydroxide to form compounds with cementitious qualities. The addition of this

**Fig. 4** The outer tube was torched to determine the composition in its wall**Fig. 5** The outer tube contained one transverse, six longitudinal, and one glass layer (dimensions in millimeters; angles denote fiber orientations with respect to longitudinal direction)

constituent provides enhanced strength, increased durability and workability, and improved finishability.

Polyvinyl butyral (PVB) is a member of the class of polyvinyl acetal resins [30]. It is derived by condensing polyvinyl alcohol (PVA) with butyraldehyde in the presence of a strong acid. PVB is completely insoluble in cement-water-mixes and is highly alkali resistant. It contains hydroxyl groups that have the potential to form a hydrogen bond between molecules, or within different parts of a single molecule. This unique feature provides remarkable changes in the surface bond strength, not only between the aggregate and the matrix, but also between the fiber reinforcement and the matrix.

The Sika ViscoCrete 2100 superplasticizer, which conformed to ASTM C494/C494M-11 [31], was added to reduce water requirements. This constituent provides excellent plasticity and workability [32]. Due to the reduced water to cement ratio, a greater ultimate strength is achieved. The addition creates a denser concrete that has less permeability and surface defects.

The styrene-butadiene-rubber (SBR) acrylic latex is a copolymer latex admixture designed as an adhesive for bond coatings, mortars and concrete. The addition of this constituent lowers the elastic modulus and significantly improves

**Fig. 6** A continuous tendon is tested in four point bending

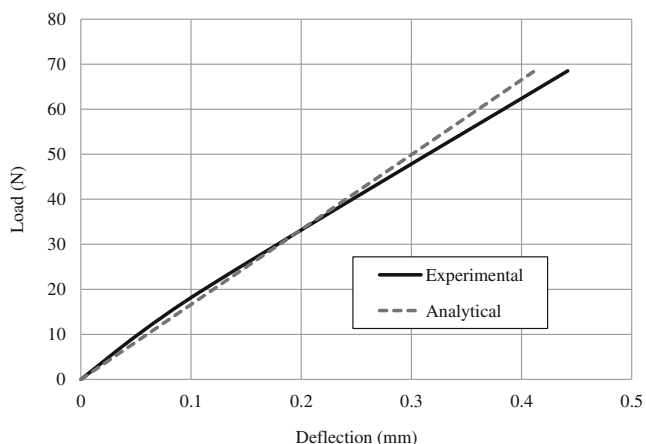


**Fig. 7** Load vs. deflection data for a 15.9 mm ID continuous tendon

the bond strength, chemical resistance, and durability of the concrete.

Typically, the type of concrete described in Table 3 reaches 90 % of its strength in 28 days; and, prior studies have shown that changes in strength and material properties are insignificant after 60 days [14]. In the present study, the original game plan called for testing the strength, material properties, and the doubly reinforced beams 28 days after placement. However, delays in design and construction of the loading frame required for testing the beams necessitated that the beam tests be conducted 120 days after placement. A decision was made to evaluate the material properties at the same time to provide a better correlation between the material properties of the concrete test articles and those associated with the doubly reinforced concrete beams.

Specifically, the micro-mechanical behavior and material properties of the final mix were evaluated under combined loading (shear and bending) by testing end-loaded cantilevers based on ASTM D747 [33]. The flexural strength corresponding to the tensile failure at the fixed support was 8.6 MPa, whereas the elastic modulus and Poisson’s ratio were 3.82 GPa and 0.25, respectively [19]. Tests conducted on the mix in accordance with ASTM C39/C39M-12 [34] revealed that it had a compressive strength of 21.7 MPa [19]. These results are summarized in Table 4.

Compared to conventional concretes, the higher stiffness ratio increases the stress transfer to the reinforcement. The relatively high Poisson’s ratio of the mix is compatible to that of the carbon reinforcement resulting in better dimensional (strain) compatibility when load (or stress) is applied.

**Table 2** Apparent laminate properties obtained from “The Laminator”

Longitudinal modulus (GPa)	105.2
Transverse modulus (GPa)	13.9
Longitudinal poisson’s ratio	0.159
Transverse poisson’s ratio	0.021

**Table 3** Mix design table

	Mix proportion (kg/m <sup>3</sup> )
Cement	710.10
HRM (Metakaolin)	42.27
PVB (Butvar B-79)	270.50
Sika	8.45
SBR (Acrylic Latex)	338.10
Water	25.36
Total	1,394.78

The material properties of the Hysol 9430 epoxy used to glue the splice within the outer tubes is listed in Table 5 [35].

**Test Setup**

Figure 8 shows a photograph of the test apparatus. The upper roller extensions were placed at a distance of 0.1524 m apart, and the lower roller extensions were placed 0.4572 m apart.

The wires from the strain gages placed within the tendons and on the free surfaces of the beam were inserted into separate channels of a data acquisition system. A quarter-bridge strain gage module (National Instruments NI 9236) was used to make the measurements and LabVIEW software was used to acquire normal strain to an accuracy of ±14 µε. Two linear variable differential transformers (LVDT’s) were used to monitor the deflection of the beam at mid-span but these results were not included in the analysis.

Displacement control was used such that the bottom platen moved upward at a rate of 1.27 mm/min. A load cell, located directly above the fixed upper platen, was used to measure force to an accuracy of ±21.7 N.

**Results and Discussion**

Due to time and cost constraints, sufficient concrete was batched to place six beams. After testing four of the beams and seeing consistent results up to the point at which the first crack occurred, it was decided to reserve the remaining two for alternate research purposes.

**Table 4** Material properties for polymer-enhanced concrete

Flexural strength (MPa)	8.6
Elastic modulus (GPa)	3.82
Poisson’s ratio	0.255
Compressive strength (MPa)	21.7



**Table 5** Material properties for Hysol 9430 epoxy

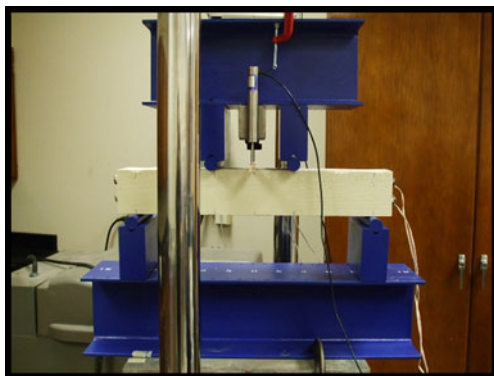
Material	Hysol 9430
Tensile modulus (GPa)	2.62
Shear modulus (GPa)	0.90
Poisson's ratio	0.350

Figure 9 shows a strain vs. displacement plot which includes curves generated from data taken from the strain gages mounted on the top and bottom surfaces of the beam. A load vs. crosshead displacement curve is also included. Figure 10, on the other hand, shows a similar plot with curves generated from data taken from strain gages placed within the upper and lower tendons. Since the test was conducted using a displacement controlled method, the abscissa reflects the time expended during the test. In this case, the crosshead moved 15.14 mm at a load rate of 1.27 mm/min making the duration nearly 12 min.

The beam remained intact until the load reached 11.64 kN when the first crack occurred. The crack developed in the central span of the beam on the lower surface and, as illustrated in Fig. 11, was observed at a distance of 60.3 mm to the left of center. The event resulted in jump discontinuities which can be observed at a crosshead displacement of 3.22 mm in the load and strain plots for the surface mounted gages (Fig. 9) and the tendons (Fig. 10).

Prior to cracking, the strains increased monotonically. The strains on the top surface and in the upper tendon were compressive while those on the lower surface and in the lower tendon were tensile. The magnitudes of the strains measured on the top and bottom surfaces, as well as those in the upper and lower tendons, were not equal when the first crack appeared because of the warpage which occurred in the cross section. Up to this point, the material behavior was construed to be linearly elastic.

Referring to the plots shown in Figs. 9 and 10, immediately after the first crack occurred, the load dropped from 11.64 kN to 8.12 kN. The strain in the upper tendon decreased slightly from  $-1,074\mu\epsilon$  to  $-851\mu\epsilon$ , whereas that in



**Fig. 8** Reinforced concrete beam situated within test apparatus

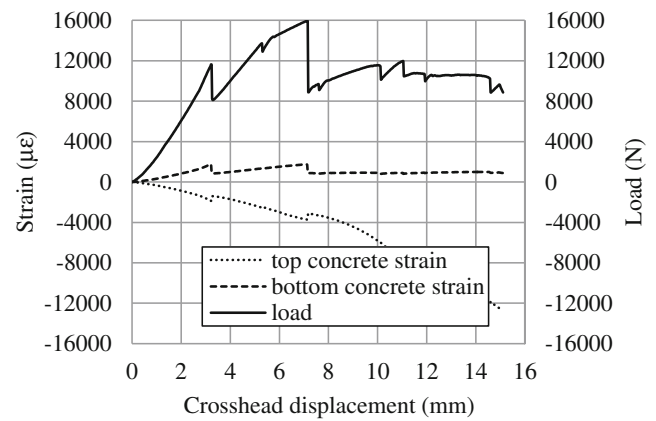


**Fig. 9** Concrete strain and load vs. crosshead displacement (beam 1)

the lower tendon significantly increased from  $1,004\mu\epsilon$  to  $1,646\mu\epsilon$ . At the same time, the strains on the upper and lower surfaces both decreased, slightly more on the lower surface.

Distinct shape changes can be seen in the strain plots when the first crack occurred. In the lower portion of the beam, the tensile strain on the bottom surface decreased (see Fig. 9) due to the crack and reduction in load. Despite the latter, the tensile strain in the lower tendon (see Fig. 10) increased. This is due to the stress transfer from the weakened concrete to the reinforcement and the upward shift in the centroid of the composite section.

The material remained relatively intact in the upper portion of the beam. Thus, the upward shift of the centroid coupled with the decrease in load, resulted in a decrease in the magnitude of the compressive strain on the top of the beam (see Fig. 9) and in the upper tendon (see Fig. 10). However, since the strain in the upper tendon remained compressive, the centroid remained below the surface on which the strain gage was installed.

Remarkably, once this stress transfer and centroid shift occurred, the load continued to increase significantly to a

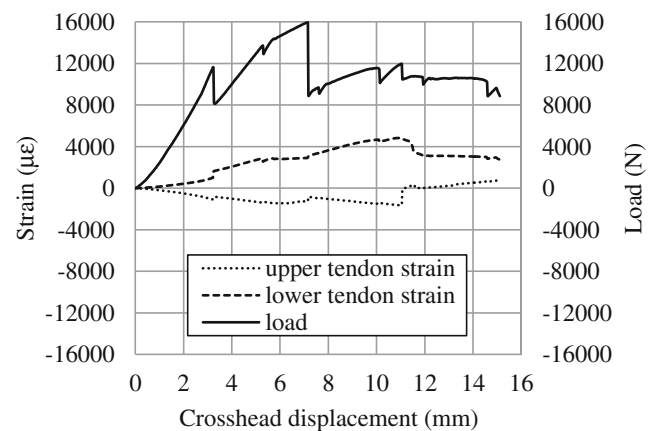


**Fig. 10** Tendon strain and load vs. crosshead displacement (beam 1)

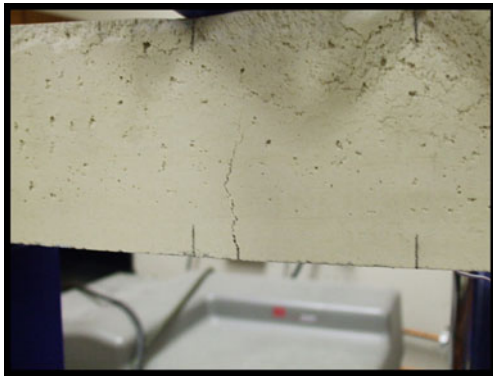


**Fig. 11** The materials remained elastic until the first crack occurred

peak value of 15.94 kN, at which point a second crack was observed (see Fig. 12). This crack developed in the central span of the beam on the lower surface, and was observed at a distance of 60.3 mm to the right of center. The second crack extended up to the top of the upper tendon, and as time went on, propagated lengthwise toward the center of the beam.

During the time between the occurrences of the first and second cracks, the magnitudes of the strains in the tendons and on the surfaces increased, except for a slight glitch observed approximately midway through the cycle. This anomaly was later attributed to slippage of the lower tendon within the concrete matrix.

Following the drop in load to 8.88 kN, created by the onset of the second crack, the load increased to 11.96 kN as the crack on the right side continually widened. During this time, the compressive strain in the upper tendon increased from  $-823\mu\epsilon$  to  $-1,646\mu\epsilon$  while the tensile strain in the lower tendon increased from  $2,901\mu\epsilon$  to  $4,825\mu\epsilon$ .

At this point, the lower tendon began to fracture which resulted in a decrease in strain from  $4,825\mu\epsilon$  to  $3,096\mu\epsilon$ . But the failure did not happen instantly; since the tendon continued to sustain a tensile strain. When the fracture occurred, the compressive strain in the upper tendon

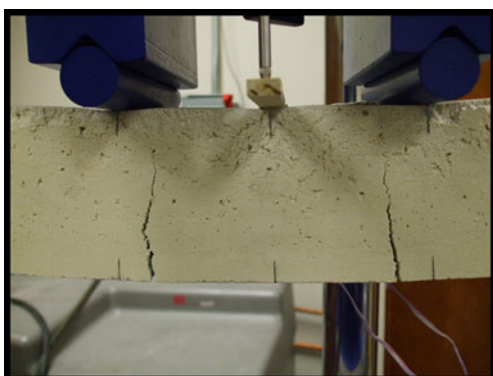


**Fig. 12** After a sharp decrease in load occurred, the load increased until a second crack developed

dropped from  $-1,646\mu\epsilon$  to  $-112\mu\epsilon$  (compressive) before gradually changing to  $321\mu\epsilon$  (tensile), and finally increasing to  $795\mu\epsilon$  when the test was halted; after 12 min when the crosshead deflection was 15.24 mm. During this portion of the loading cycle, the strain on the bottom surface remained fairly constant at about  $950\mu\epsilon$ , since the central section was completely segmented. At the same time, the strain on the top surface became progressively higher and increased to  $-12,380\mu\epsilon$  as the stresses were transferred to this region.

The change in sign of the strain that occurred in the upper tendon indicated that, when the lower tendon fractured, the neutral axis shifted even further towards the top of the beam, beyond the inside portion of the upper tendon where the gage was located. At this point, both tendons were in tension; albeit the lower tendon had already fractured. The minor glitches in the strain plots extracted from the tendons were later attributed to lateral movement (slippage) which occurred as the bonds between the tendons and the concrete matrix broke.

It is significant to note that the beam sustained a load only slightly less than that which corresponded to the first crack (11.64 kN) despite appreciable deformation and readily observable damage that was observed. This remarkable performance was attributed mainly to the symmetrical distribution of the tendons in the section and partly to the expansion joints created by placing the splices in them. The result was so unexpected that a decision was made to extend the duration of the next three tests to see how much deformation a beam could really take before it was readily apparent that it would collapse.

Figure 13 shows a superposition of load vs. deflection plots corresponding to the four beams tested. It is readily apparent that these curves provide a measure of structural integrity as well as valuable clues regarding how damage took place and progressed. A similar conclusion can be reached regarding the output from the strain gages.

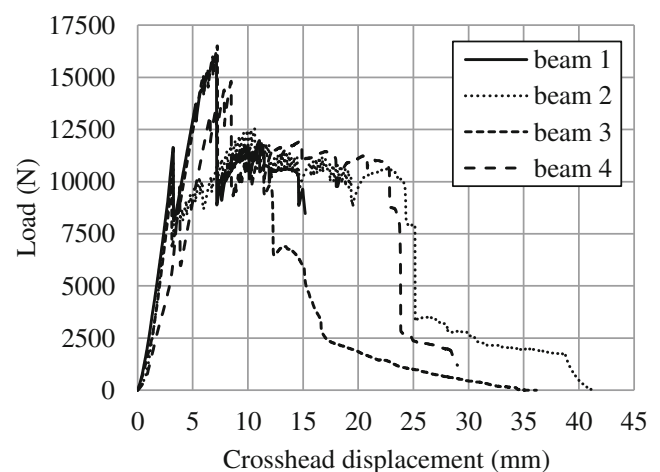


**Fig. 13** Load vs. crosshead displacement of the four beams

For the four beams tested, the first crack appeared in the same general location relative to the beam center and the average load to failure was 10.61 kN. Although the second crack appeared in the same general location relative to the beam center, the corresponding crosshead displacement was not as consistent, from beam to beam, as it was for the first crack. Following the second crack, all of the beams held a load approximately equal to that which corresponded to the first crack, albeit the structural behavior in this regime varied considerably.

The sections which follow describe how a finite element model was produced to characterize the structural behavior in the elastic range and how a hybrid approach can be used for structural analysis.

### Finite Element Modeling

A finite element model was developed to quantify the structural behavior of the beams while they remained within the elastic range. The analysis was performed in NX Nastran and Patran 2010 using the “linear elastic” constitutive model. The model was developed using FEMAP, imported into Patran, solved in Nastran, and then post processed in Patran.

The 0.4572 m long beam section was simply supported on the bottom at both ends over its width. As shown in Fig. 8, these locations coincided with the positions of the bottom rollers of the loading frame used to test the beams. The center of the right roller was fixed to enable the model to run.

During the simulation, one half of the load was distributed over the width of the beam at locations that corresponded to the positions of the upper rollers. The concrete was modeled using a solid hexagonal element called CHEX8 as an isotropic material having the properties listed in Table 4.

A “laminated” model was used to characterize the carbon fiber tendons based on the lamina material properties listed in Table 2. A relatively crude model was built for the tendons by neglecting the glass layers in the outer tubes and the center joint between them by making the tubes continuous across the span. The glue-filled gaps between the outer tubes and the splices were also neglected, and each splice was modeled by adding the layers it contained directly beneath the inner surface of the outer tube.

### Finite Element Analysis (FEA) – Longitudinal, Normal Strain

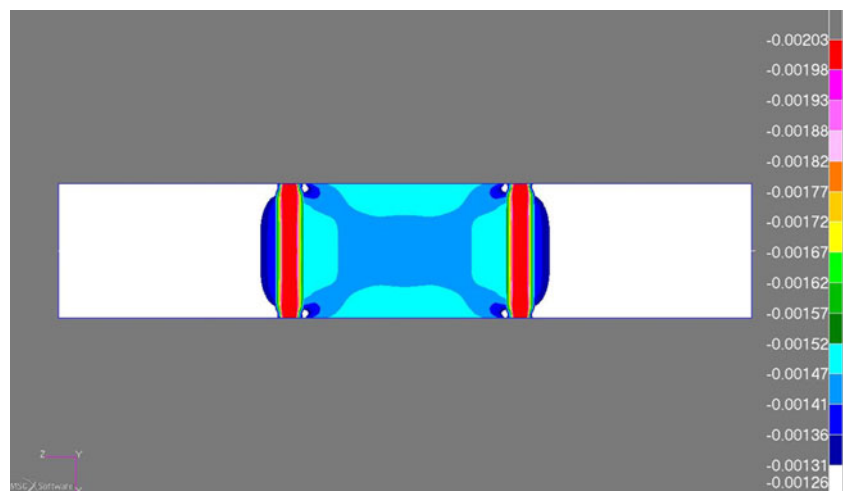
The finite element model was run for a simulated load case of 10.61 kN which corresponded to the average load to the first crack found for beams 1 through 4. As mentioned earlier, uniaxial strain gages were mounted in the longitudinal direction on the inner surfaces of the upper and lower tendons adjacent to the splice, at a distance of 26.0 mm from the center span of the beam. The tendons were rotated so that the gages were located at the furthest distances possible from the neutral axis of the composite cross section.

So that direct comparisons could be made with the strain gage data, normal strains were computed along the longitudinal axes of the beam and tendons. Contour plots were generated to illustrate the strain gradient for the regions of interest.

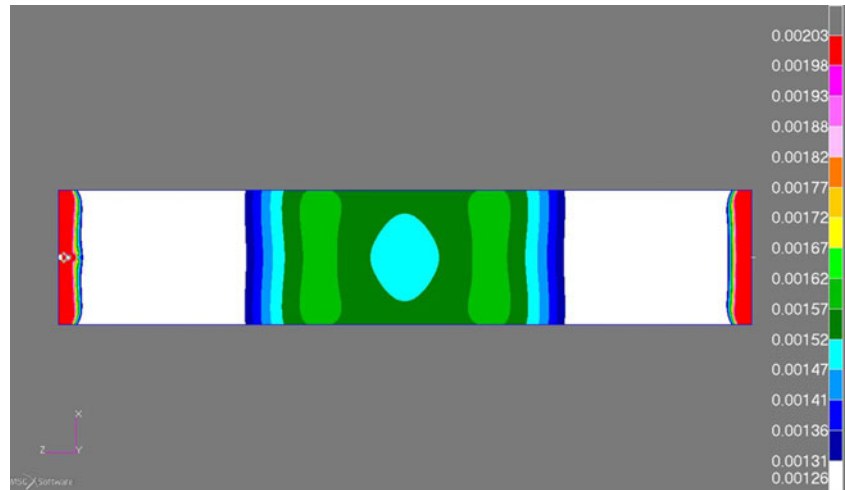
In these plots, positive and negative values correspond to tensile and compressive strains, respectively. The strains do not all correspond to principal values, since some results are presented beneath supports at which shear stresses exist; and, others correspond to inter-laminar strains.

Figure 14, for example, shows a contour plot of the longitudinal, normal strain in the concrete on the top surface of the beam. In this case, the observer is looking directly

**Fig. 14** Longitudinal, normal strain in the concrete on the top surface of the beam



**Fig. 15** Longitudinal, normal strain in the concrete on the lower surface of the beam



downward. The range for the strains was limited in this rendition to accentuate the strain gradient in the region located between the upper supports. The color key shown to the right in the figure corresponds to the strain level. The largest strain, occurs directly beneath the upper supports (see Fig. 2) due to the high contact stresses which occur there. The longitudinal, normal strain at the center of the span where the strain gage was located is  $-1,415\mu\epsilon$ . The latter corresponds to one of the three principal strains.

A similar plot, tailored to show the strain gradient in the concrete located between the rollers on the bottom surface of the beam is shown in Fig. 15. However, in this case, the observer is looking directly upward. The range and color key are identical to those employed in Fig. 14 but the strains are of opposite sign. The largest strain, occurs directly above the lower supports (see Fig. 2) due to the high contact stresses which occur there. The longitudinal, normal strain at the center of the span where the strain gage was located is  $1,474\mu\epsilon$ . The latter corresponds to one of the three principal strains.

**Fig. 16** Longitudinal, normal strain on the top half of the inner surface of the upper tendon

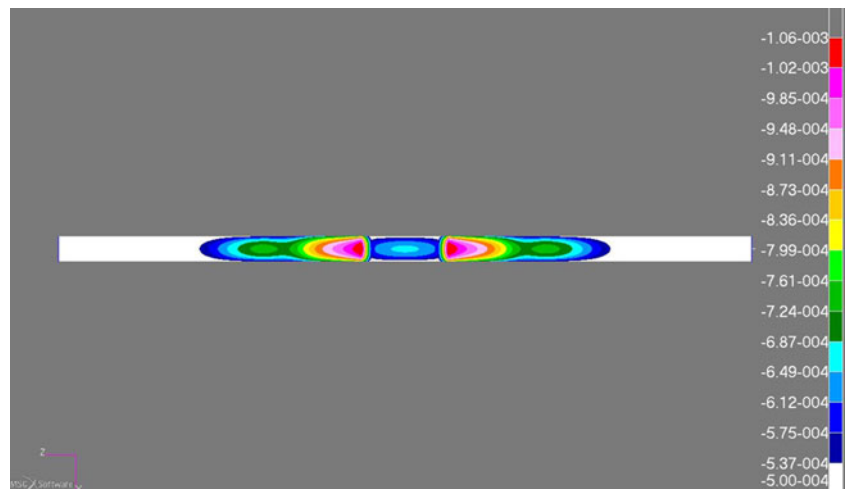
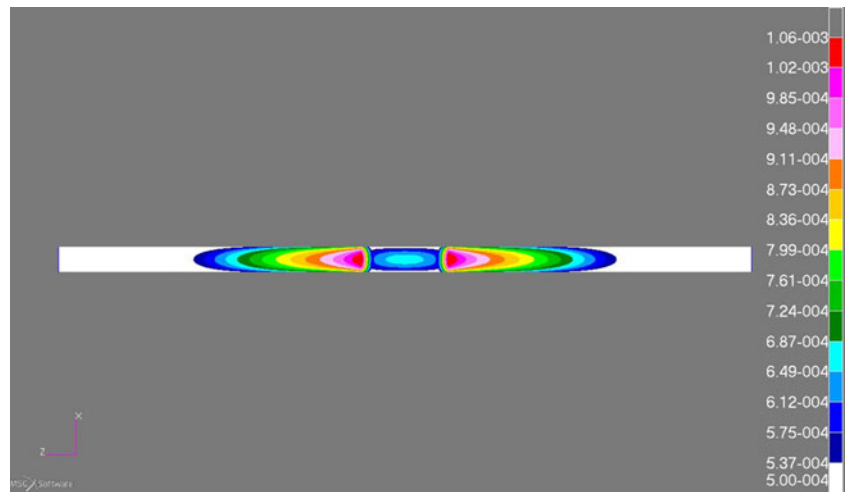


Figure 16 shows a contour plot of the longitudinal, normal strains on the top half of the inner surface of the upper tendon. In this case, the observer is looking directly downward. The longitudinal, normal strain at the point on the free surface where the strain gage was located is  $-937\mu\epsilon$ . The latter corresponds to one of the principal strains. It should be noted, however, that the strains in the central portion of the figure where the splice is located are inter-laminar, since the layers of the splice lie directly below the innermost layer of the outer tube.

Figure 17, on the other hand, shows a contour plot of the longitudinal, normal strains on the bottom half of the inner surface of the lower tendon. However, in this case, the observer is looking directly upward. The range and color key are identical to those employed in Fig. 16 but the strains are of opposite sign. The longitudinal, normal strain at the point on the free surface where the strain gage was located is  $942\mu\epsilon$ . The latter corresponds to one of the principal strains. Again, the strains in the central portion of the figure where the splice is located are inter-laminar.

**Fig. 17** Longitudinal, normal strain on the bottom half of the inner surface of the lower tendon



**Comparison Between Experimental and Analytical Results**

Comparisons were made between the experimental data and analytical results. This was done initially by generating load vs. strain plots up to the point at which the first crack occurred.

Figures 18(a) and (b), for example, show plots corresponding to load vs. strain data taken from the gages placed on the top and bottom concrete surfaces, respectively, of the four beams tested. The plots labeled FEA (finite element analysis) were generated by running the finite element program with the average load to failure.

Figures 19(a) and (b), on the other hand, show plots corresponding to load vs. strain data taken from the gages placed within the upper and lower tendons, respectively. FEA plots are included for each case.

The experimental and analytical plots match fairly well considering that the model was relatively crude. The deviation seen in the results presented for the lower tendon may be due to the fact that the center joint in the outer tubes was neglected. Since the upper tendon is in compression, the tubes butt up against one another making it seem as if the

tendon is continuous. In contrast, the lower tendon is in tension, thereby stretching the joint.

Other comparisons were made based on the average load at which the first crack occurred. Table 6 summarizes the results for this loading condition. The percentage errors listed in the table were calculated using the finite element results as a baseline. Considering the scatter in experimental data, the model performed well.

Comparisons were also made regarding crack location. Referring to Fig. 15, the finite element model predicted that the maximum longitudinal strain in the concrete on the bottom of the central span was  $1,585\mu\epsilon$ . This occurred along the longitudinal centerline (half way across the width) at a distance of 57.2 mm to the right and left of center span. Close inspection of the spent beams indicated that cracks initiated at this location and subsequently propagated through the thickness until they appeared on the sides of the specimens at a distance of 60.3 mm from the center span (see Figs. 11 and 12). This was an exact match.

Finally, the maximum principal stress predicted by the finite element model at the critical locations was 6.07 MPa. The latter is considerably less than the flexural strength measured for the concrete (8.6 MPa; see Table 4) but this

**Fig. 18** Load vs. top concrete strain (a) and bottom concrete strain (b) in the four beams, to first crack

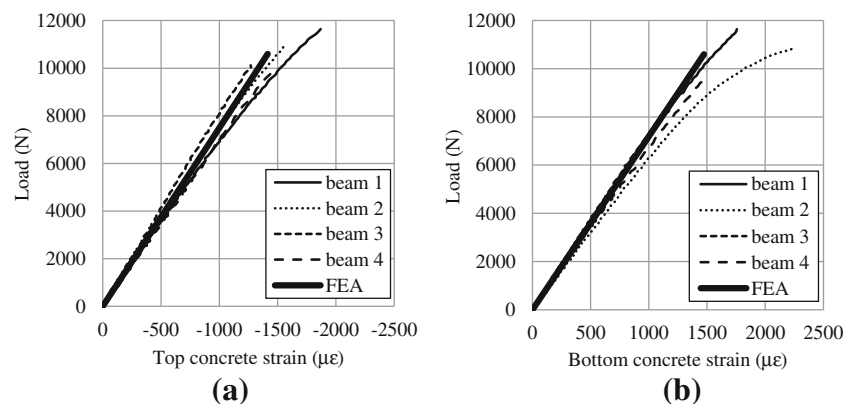
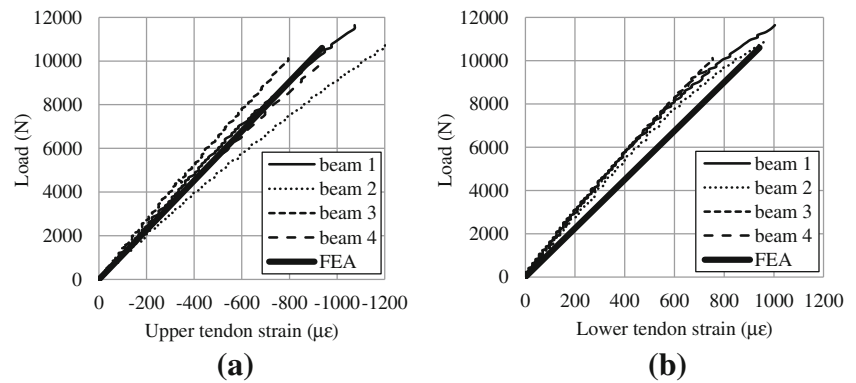


**Fig. 19** Load vs. upper tendon strain (a) and lower tendon strain (b) in the four beams, to first crack



should be expected, since a larger area is affected by the critical stress in a beam subjected to four point bending as compared to one which is cantilevered and end loaded.

In general, the finite element model predicted slightly lower strains on the concrete surfaces than those measured by the gages. The implication is that the stiffness ratio was incorrect or that the modeling parameters and/or assumptions made during the process created an overly stiff structure. A more sophisticated model which included the glue-filled joints and glass layers may help to solve and/or diagnose the root of this problem but many other factors could have contributed to the error.

It is evident in Fig. 7, for example, that “The Laminator” predicted a higher stiffness for the outer tube than that measured. Since the effective properties produced by the “laminator” model within Patran agreed with those obtained from “The Laminator,” the same trend would hold true when the input properties were incorporated into the beam model.

Modeling geometry also increased the stiffness of the model. Butting the layers which constituted the splice directly below the inner surface of the outer tube effectively increased both the inner and outer diameters of the splice, thereby increasing the moment of inertia and the flexural stiffness associated with the tendons.

Factors which could have influenced the experimental results include misalignment of the tendons and gages as well as shrinkage, voids, sedimentation, and non-linear behavior of the cementitious matrix. For a given beam, these could be taken into account by tuning the finite element

model with the data extracted from the strain gage system or by making the model more sophisticated, for example, by incorporating an iterative procedure to account for things like changes in the elastic modulus with strain.

Alternatively, improved prefabrication of the tendon and mold would guarantee precise placement of the strain gages and the tendons within the cross section. Amplification of the vibrating table may help to reduce voids and decrease concrete aggregate separation within the cross section.

### Hybrid Approach

The development of the finite element model is advantageous, since it enables the user to obtain a global perspective of the stress distribution. This allows a hybrid approach to be taken in which finite element results are synthesized with experimental measurements. As demonstrated in the present study, the hybrid approach can be used to correlate data taken at a given location to the critical stress at the point of failure. Perhaps more importantly, it could be used to predict the displacements, strains, and stresses at every point in the structure based on the output from a single strain gage.

### Conclusions

This paper showed how surface mounted strain gages were used to monitor reinforced concrete beams constructed by placing a flexible, polymer-enhanced cementitious matrix

**Table 6** Strain data measured for first crack compared to FEA results generated for average load

	Beam 1	Beam 2	Beam 3	Beam 4	Average	FEA Results	% Error
Load (kN)	11.64	10.88	10.12	9.75	10.60	10.60	–
Top concrete strain ( $\mu\epsilon$ )	–1,869	–1,576	–1,297	–1,436	–1,545	–1,415	9.2
Bottom concrete strain ( $\mu\epsilon$ )	1,757	2,259	1,436	1,492	1,736	1,474	17.8
Upper tendon strain ( $\mu\epsilon$ )	–1,074	–1,255	–795	–920	–1,011	–937	7.9
Lower tendon strain ( $\mu\epsilon$ )	1,004	976	753	753	872	942	–7.4

over relatively stiff hollow graphite tendons. The tendons were equipped with strain gages mounted on their inner walls and materials were placed symmetrically so that the composite section could potentially resist reverse loadings.

The primary purpose of embedding the gages within the tendons was to characterize the structural behavior and insure that the stress in the materials remained within the elastic range so that damage did not occur. However, the beams were tested well beyond this point to demonstrate how the strains obtained from the structural information system could be used to characterize structural performance, once the first crack occurred.

During the experimental tests, the first crack developed in the central span at the lower surface of the beam. The crack was detected by the gages and seen as jump discontinuities in the load and strain plots for the surface mounted gages as well as the tendons. A finite element model was developed to characterize the structural response in the elastic range and comparisons were made between the experimental and analytical results. The development of the finite element model provided a global perspective of the stress distribution which was employed in a hybrid approach to understand and validate the onset of the first crack.

The ability to characterize structural performance beyond the elastic range was also demonstrated by analyzing data obtained from displacement-controlled tests. Splices in the tendons and slippage between them and the cementitious matrix helped to prevent sudden collapse and allowed the composite structure to withstand relatively high service loads despite appreciable deformation.

**Acknowledgments** The authors would like to thank the United States Army Research, Development, and Engineering Center (AMRDEC) of the Research, Development, and Engineering Command (RDECOM) at Redstone Arsenal in Huntsville, Alabama, for supporting this research under the Department of Defense (DOD) SBIR Contract No. W31P4Q-05-C-R103. Portions of the study were also funded by the U.S. Department of Commerce under NOAA SBIR Contract No. WC133R-09-CN-0108. The authors would also like to thank Mr. Ravi K. Bommu for his work involving tendon development, Drs. Thomas Lavin and Bo Xu for their contributions to concrete development, and Mr. Rajesh Vuddandam for his contribution to beam testing with the data acquisition system. Any opinions, findings, conclusions or recommendations expressed in this publication are those of the authors and do not necessarily reflect the views of the funding agencies previously mentioned.

## References

- Hexcel Corporation (2005) Prepreg technology, publication no. FGU 017b, March; online at: [http://www.hexcel.com/Resources/DataSheets/Brochure-Data-Sheets/Prepreg\\_Technology.pdf](http://www.hexcel.com/Resources/DataSheets/Brochure-Data-Sheets/Prepreg_Technology.pdf)
- U.S. Department of Defense (2002) Composite materials handbook, volume 2: polymer matrix composites materials properties, MIL-HDBK-17-2 F, June 17, pp. 4-41 and 4-63
- Teng J (2001) FRP composites in civil engineering, volumes 1–2, Elsevier. ISBN 978-0-0804-3945-7
- Biszick KR, Toutanji HA, Gilbert JA, Marotta SA, Ooi TK (2006) Evolution of strategically tuned absolutely resilient structures (STARS). Proc. of SEM Annual Conference & Exposition on Experimental and Applied Mechanics, Saint Louis, Missouri, Paper No. 32, 7 pages
- Biszick KR, Gilbert JA (1999) Designing thin-walled, reinforced concrete panels for reverse bending. Proc. of the SEM Spring Conference on Theoretical, Experimental and Computational Mechanics, Cincinnati, Ohio, pp. 431–434
- Vaughan RE, Gilbert JA (2001) Analysis of graphite reinforced cementitious composites. Proc. of the SEM Annual Conference and Exposition, Portland, Oregon, pp. 532–535
- Ooi TK, Gilbert JA, Bower MV, Vaughan RE, Engberg RC (2005) Modal analysis of lightweight graphite reinforced silica/polymer matrix composite plates. Exp Mech 45(3):1–5
- Ooi TK, Engberg RC, Gilbert JA, Vaughan RE, Bower MV (2004) Modal testing of a lightweight cementitious structure. Experimental Techniques, November/December, pp. 37–40
- Badr A, Ashour AF, Platten AK (2006) Statistical variations in impact resistance of polypropylene fibre-reinforced concrete. Int J Impact Eng 32(11):1907–1920
- Binek LA, Gilbert JA, Ooi TK, Bower MV, Biszick KR (2007) Ballistic testing of STARS. Proc. of SEM Annual Conference & Exposition on Experimental and Applied Mechanics, Springfield, Massachusetts, Paper No. 196, 10 pages
- Xu B, Toutanji H, Gilbert JA (2010) Impact resistance of poly (vinyl alcohol) fiber reinforced high-performance organic aggregate cementitious material. Cement Concr Res 40:347–351
- Lavin T, Toutanji H, Xu B, Ooi TK, Biszick KR, Gilbert JA (2008) Matrix design for strategically tuned absolutely resilient structures (STARS). Proc. of SEM XI International Congress on Experimental and Applied Mechanics, Orlando, Florida, Paper No. 71, 12 pages
- Toutanji H, Xu B, Gilbert JA, Lavin T (2010) Properties of poly (vinyl alcohol) fiber reinforced high-performance organic aggregate cementitious material: converting brittle to plastic. Construct Build Mater 24(1):1–10
- Xu B, Toutanji HA, Lavin T, Gilbert JA (2011) Characterization of poly(vinyl alcohol) fiber reinforced organic aggregate cementitious materials. Polym Concr 666:73–83
- RockTest Limited, Saint-Lambert, Quebec, Canada (2005) Instrumented rebar and sister bar, Model IRHP and IRCL. Data sheet available on the web at: [http://www.roctest-group.com/sites/default/files/datasheets/products/IRHP-E50138-W\\_0.pdf](http://www.roctest-group.com/sites/default/files/datasheets/products/IRHP-E50138-W_0.pdf), pp. 1–2
- Encardio-rite Electronics, Lucknow, India (2008) Model EDS-12 V vibrating wire sister bar strain meter. Product sheet available on the web at: [http://www.encardio.com/consolidated2011-12\\_eng.pdf](http://www.encardio.com/consolidated2011-12_eng.pdf), p. 15
- Sanchez J, Andrade C, Fulla J (2010) Hydrothermal monitoring using embedded sensors of the actual roof system of the Prado museum. Construct Build Mater 24(12):2579–2589
- Bommu RK (2010) Development of instrumented tendons for embedment in a structural information system. Master's Thesis, Department of Mechanical and Aerospace Engineering, University of Alabama in Huntsville
- Biszick KR (2010) Design of a structural information system (SIS) for strategically tuned absolutely resilient structures (STARS). Ph.D. Dissertation, Department of Civil and Environmental Engineering, University of Alabama in Huntsville
- Biszick KR, Gilbert JA, Toutanji H, Lavin T, Britz MT, Bommu RK (2011) Characterization of adaptive reinforced concrete structures, Proc. of SEM Annual Conference & Exposition on Experimental and Applied Mechanics, Uncasville, Connecticut, Paper No. 124, 12 pages
- Wootton IA, Spainhour LK, Yazdani N (2003) Corrosion of steel reinforcement in carbon fiber-reinforced polymer wrapped concrete cylinders. J Compos Construct 7(4):339–347

22. U.S. Department of Defense (2002) Composite materials handbook, volume 2: Polymer matrix composites materials properties, MIL-HDBK-17-2 F, June 17, pp. 4–110 – 4–116
23. Benenson W, Harris JW, Stocker H, Lutz H (2002) Handbook of physics. SPRINGER, New York, pp 233–241
24. ASTM C78/C78M-10 (2010) Standard test method for flexural strength of concrete (using simple beam with third-point loading). Available on the web at: <http://www.astm.org/Standards/C78.htm>
25. Hexcel Corporation, 3501-6 Epoxy matrix product data sheet, Pleasanton, CA. Available on the web at: [http://www.hexcel.com/Resources/DataSheets/Prepreg-Data-Sheets/3501-6\\_eu.pdf](http://www.hexcel.com/Resources/DataSheets/Prepreg-Data-Sheets/3501-6_eu.pdf)
26. Talreja R, Yalvac S, Yates LD, Wetters DG (1992) Transverse cracking and stiffness reduction in cross ply laminates of different matrix toughness. *J Compos Mater* 26:1647
27. Lindell M (2006) The laminator - classical analysis of composite laminates. Version 3.6 program shareware available on the web at: <http://www.thelaminator.net>
28. ASTM C150/C150M-11 (2011) Standard specification for Portland cement. Available on the web at: <http://www.astm.org/Standards/C150.htm>
29. ASTM C618-08A (2008) Standard specification for coal fly ash and raw or calcined natural pozzolan for use in concrete. Available on the web at: <http://www.astm.org/Standards/C618.htm>
30. Mark JE (1999) Polymer data handbook. Oxford University Press, Inc., pp. 910-912
31. ASTM C494/C494M-11 (2011) Standard specification for chemical admixtures for concrete. Available on the web at: <http://www.astm.org/Standards/C494.htm>
32. Sika® ViscoCrete® 2100: High range water reducing admixture: Product data sheet identification no. 781-540 (2005), Sika Corporation, Lyndhurst, New Jersey, pp. 1–2. Available on the web at: <http://us01.webdms.sika.com/fileshow.do?documentID=52>
33. ASTM D747-10 (2010) Standard test method for apparent bending modulus of plastic by means of a cantilever beam. Available on the web at: <http://www.astm.org/Standards/C494.htm>
34. ASTM C39/C39M-12 (2012) Standard test method for compressive strength of cylindrical concrete specimens. Available on the web at: <http://www.astm.org/Standards/C494.htm>
35. On Hand Adhesives, Inc. (2012) Hysol 9430. Available on the web at: <http://www.gluguru.com/Hysol%20Data%20Sheets/9430.htm>